Journal Pre-proof

Three-dimensional simulation of horseshoe vortex and local scour around a vertical cylinder using an unstructured finite-volume technique

Wei Zhang, Miguel Uh Zapata, Xin Bai, Damien Pham-Van-Bang, Kim Dan Nguyen

PII: S1001-6279(19)30043-5

DOI: https://doi.org/10.1016/j.ijsrc.2019.09.001

Reference: IJSRC 254

To appear in: *International Journal of Sediment Research*

Received Date: 25 January 2019

Revised Date: 19 August 2019

Accepted Date: 22 September 2019

Three-dimensional simulation of horseshoe vortex and local scour around a vertical cylinder using an unstructured finite-volume technique

Wei Zhang[a], Miguel Uh Zapata[b], Xin Bai[a], Damien Pham-Van-Bang[c], Kim Dan Nguyen [a,*]

[a] *Laboratory for Hydraulics Saint-Venant (LHSV, ENPC-EDF R&D-Cerema), Université Paris-Est, 6 quai Watier, BP 49, 78401 Chatou Cedex, France*

[b] *CONACYT, Centro de Investigación en Matemáticas A.C., (CIMAT), Unidad Mérida, Sierra Papacal, CP, Mérida, Yucatan 97302, Mexico*

[c] *Laboratory for Hydraulics and Environment (LHE), Institut National de la Recherche Scientifique, Université du Québec, 490 rue de la Couronne, G1K 9A9 Québec (QC), Canada*

Corresponding author: kimdan_nguyen@yahoo.fr

ABSTRACT

A Large Eddy Simulation model is developed to simulate the hydrodynamics and scour process around a circular cylinder. The Navier-Stokes solver is based on the projection method and a second-order unstructured finite-volume method. A sigma-coordinate system is used to obtain an accurate representation of the evolution of the sediment-water interface. Bed erosion is simulated by solving the sediment continuity equation using a mass-conservating sand-slide algorithm and a bedload transport rate, which is based on a description of physical processes (Engelund & Fredsøe, 1976). Simulations of flow around a vertical cylinder for free-slip bed, rigid bed, and live-bed cases are done. The mean velocity profile and shear stress validate the accuracy of this model. Horseshoe vortex and lee-wake vortex shedding structure are simulated, and the results are thoroughly discussed in depth. The formation and the temporal development of the scour hole and other topographic bed features are successfully reproduced. The current paper reports the first known investigation of both scour evolution and coherent structure using large-eddy simulation.

Key words: Non-hydrostatic flows, Horseshoe vortex, Wake region, Scouring, Bedload transport.

Three-dimensional simulation of horseshoe vortex and local scour around a vertical cylinder using an unstructured finite-volume technique

1. Introduction

One well-known difficulty with regard to scour studies is the local description of flow properties close to singularities (Baker, 1979; Dargahi, 1990; Kirkil et al., 2008; Kirkil & Constantinescu, 2010, 2015; Nishioka & Sato, 1974; Park, et al., 1998; Williamson, 1989). Indeed, due to the presence of obstacles, the flow forms a Horseshoe Vortex (HV) system upstream and a boundary layer detachment as well as complicated vortex shedding at the wake of the structure. These features of the problem significantly affect the scour as it evolves around the cylinder.

Due to the progress in the availability of computational power, numerical studies on scour around a vertical cylinder are now well-documented. However, the development of accurate and efficient models for the scour process is still a complicated task. First, hydrodynamic and sediment transport models are coupled such that a closure equation for the bedload estimation is required. Second, the sand-slide processes play an important role during the formation of a scour hole, thus, the local bed slope and friction angle of the bed material should be incorporated in the model. Third, a mesh adaptation around the cylinder boundary is required to capture the bed deformation (Khosronejad et al., 2011, 2012). Finally, turbulence models are necessary to simulate the coherent structures of flow fields with the presence of a HV system. These factors must be overcome if better models are to be obtained.

Roulund et al. (2005) presented a major advance in simulating local scour around a vertical cylinder by using a structured finite volume code to solve the Reynolds Averaged Navier-Stokes (RANS) equations with a k–ω turbulence closure (where k is the turbulent kinetic energy and ω is the specific dissipation rate). Overall, their numerical results coincide with their experimental data and the study is frequently referenced in many studies (Baykal et al., 2014, 2017; Stahlmann, 2013; Zhou, 2017). The work of Kirkil et al. (2008) and Kirkil & Constantinescu (2010, 2015) applied a Large-Eddy Simulation (LES) to analyze the coherent structure of flow fields with the presence of a HV system upstream and a wake region behind a vertical cylinder. However, their simulations started from an equilibrium hole obtained from experimental results such that no scour evolution was analyzed. Khosronejad et al. (2011, 2012) developed a Fluid-Structure Interaction Curvilinear Immersed Boundary (FSI-CURVIB) method with a k-ω closure model. Their work has shown that the bluntness of the pier significantly influences the predictive capabilities of models. Link et al. (2012) used a Detached-Eddy Simulation (DES) to simulate scour hole evolution around circular and rectangular piers. More recently, Nagel (2018) used a Eulerian two-phase model to study the live bed erosion around a cylinder.

In the current paper, a 3D numerical study is presented on local scour around a vertical cylinder using the Engelund and Fredsøe (1976) bedload formula applied to the simulations done by Roulund et al. (2005), which is classified as a live bed case (Melville & Chiew, 1999). A second-order unstructured finite-volume model combined with a sigma-coordinate system is applied to describe the dynamic shape of the sediment-water interface. In order to prevent the bed slope from exceeding the angle of repose for the sediment material, a mass conservating sand-slide model is developed. Large Eddy Simulation is applied to simulate the HV-system structure at the base of a vertical cylinder. Large-scale coherent structures in the presence of an HV system in the near-bed region as well as vortex shedding in the wake region are observed and discussed here. Table 1 provides highlights of the current study by giving an overview of different terms handled in the previously cited studies. The current paper reports the first known investigation of both scour evolution and coherent structures using a finite volume method.

The current paper is organized as follows. The second section introduces the hydrodynamic model. The third section presents the morphodynamic model in a sigma-coordinate system including the bedload estimation and sand-slide model. The fourth section summarizes the numerical techniques used in the simulation. The fifth section presents the numerical simulations. Finally, the last section gives the conclusions and offers suggestions for future research.

2. The hydrodynamic and SubGrid-Scale modeling

The Navier-Stokes equations are filtered with an implicit spatial filter of characteristic space size. The resulting equations are given by:

$$\frac{\partial \overline{u}_i}{\partial x_i} = 0, \tag{1}$$

$$\frac{\partial \overline{u}_i}{\partial t} + \frac{\partial}{\partial x_j}\overline{u}_i\overline{u}_j = -\frac{1}{\rho}\frac{\partial \overline{p}}{\partial x_i} + \frac{\partial}{\partial x_j}\left[\nu\left(\frac{\partial \overline{u}_i}{\partial x_j} + \frac{\partial \overline{u}_j}{\partial x_i}\right)\right] - \frac{\partial \tau_{ij}^{sg}}{\partial x_j}, \tag{2}$$

where x_i (i=1,2,3) are (x,y,z), respectively, are the Cartesian coordinates, the bar over the variables denotes filtering, $\overline{u}_i$ are the resolved velocity components of the velocity vector, $\overline{p}$ is the resolved pressure, and

$$\tau_{ij}^{sg} = \overline{u_i u_j} - \overline{u}_i\overline{u}_j, \tag{3}$$

is the Sub-Grid Stress (SGS) tensor used to take into account the effect of unresolved length scales.

As suggested by Smagorinsky (1963), the smallest turbulent eddies are almost isotropic and the Boussinesq eddy viscosity assumption can be used to provide an accurate approximation of the effects of these unresolved smallest eddies. According to the Boussinesq assumption, the momentum transfer caused by turbulent eddies can be modeled with an eddy viscosity, and the relations between the eddy viscosity and the sub-grid stress tensor can be described as:

$$\tau_{ij}^{sg} = -2\nu_t \overline{S_{ij}} + \frac{1}{3}\tau_{ii}^{sg}\delta_{ij}, \tag{4}$$

where δ_{ij} is the Kronecker delta, $\overline{S_{ij}} = \frac{1}{2}\left(\frac{\partial \overline{u}_i}{\partial x_j} + \frac{\partial \overline{u}_j}{\partial x_i}\right)$ is the resolved rate-of-strain tensor, and ν_t is the SGS viscosity:

$$\nu_t = l_{sg}^2 \left|\overline{S}\right|, \tag{5}$$

where $\left|\overline{S}\right| = (2S_{ij}S_{ij})^{1/2}$, and l_{sg} is the sub-grid length scale. In the near wall region, the length scale of the sub-grid scale motions cannot be described with a constant value but will decrease as the wall is approached. Thus, a wall damping function must be implemented in addition to the standard Smagorinsky SGS model to capture this boundary layer effect. In the current study, the near wall damping model of Mason and Thomson (1992) is used to achieve a modified length scale, described by:

$$\frac{1}{l_{sg}^n} = \frac{1}{(C_s\Delta)^n} + \frac{1}{(\kappa l_w)^n}, \tag{6}$$

where n is the Mason wall matching power, taken as 2, C_s is the Smagorinsky constant, Δ is the average spacing $\Delta = V^{1/3}$ with V being the volume of the element, and κ is the von Karman constant, and l_w is the distance from the center of a control volume to the wall. The value of C_s = 0.1 previously proposed for channel flow (Deardorff, 1970) is used in the current study, where strong anisotropic turbulence occurs in the near-wall region.

In the current study, non-dimensional governing equations for the flow are derived using the mean velocity, U, and the cylinder diameter, D, as velocity and length scales, respectively. The Reynolds number based on the cylinder diameter is defined as $Re_D = UD/\nu$.

3. The bed morphodynamic model

The current study is focused on the numerical simulation of bedload transport and the suspended load is negligible. The free surface also is ignored because small Froude numbers are accounted for in the proposed model (Roulund et al., 2005). The bed morphodynamic model includes the Exner-Polya equation, the bedload estimation, and the sand-slide model.

3.1. The Exner-Polya equation

The bed evolution caused by bedload transport is given by the Exner-Polya equation (Yalin, 1977):

$$(1-\eta)\frac{\partial z_b}{\partial t} + \nabla \cdot q_b = 0\,. \tag{7}$$

Where $z_b(x,y,t)$ is the local bed level, η is sediment material porosity, and q_b is the bedload transport rate depending on the hydraulic and sediment variables. The porosity of the granular material correlates to the particle arrangement (close and random) and monodispersity of materials. For really monodisperse material of identical beds, the solid volume fraction could vary between 0.54 and 0.74 depending on the cubical arrangement or maximum hexahedral packing. With preparation of the sediment bed in water, the value usually is 0.6 and porosity η is taken as 0.4 (Pham Van Bang et al., 2008). The model to calculate q_b is described in the next section.

3.2. *Bedload estimation*

A two-dimensional bedload formula proposed by Engelund and Fredsøe (1976) is applied. The bedload transport rate, q_b, is given by:

$$q_b = \frac{1}{6}\pi d^3 \frac{p_{EF}}{d^2} U_b, \quad p_{EF} = \left[1 + \left(\frac{\frac{1}{6}\pi\mu_d}{\theta - \theta_c}\right)^4\right]^{-1/4}, \quad U_b = aU_f(1 - 0.7\sqrt{\theta_c / \theta}), \tag{8}$$

where d is the grain size, p_{EF} is the percentage of particles in motion on the bed surface, U_b is the mean velocity of a moving sediment particle, U_f is the friction velocity, μ_d = 0.51 represents the dynamic friction coefficient corresponding to value 27° for the angle of repose of sediment material, θ is the Shields parameter associated with the skin friction, θ_c is the critical value of θ for the initiation of sediment motion on the bed, and a is an empirical constant. Experimental predictions are generally good for a = 10 and a suitable choice of θ_c (Fernandez Luque & van Beek, 1976; Meland & Norrman, 1966). The critical Shields parameter is calculated by:

$$\theta_c = \theta_{c0}\left(\cos\beta\sqrt{1 - \frac{\sin^2\alpha\tan^2\beta}{\mu_s^2}} - \frac{\cos\alpha\sin\beta}{\mu_s}\right), \tag{9}$$

where θ_{c0} is the critical Shields parameter for a horizontal bed, taken as 0.05, μ_s is the static friction coefficient, taken as μ_s = 0.63 for sand (Roulund et al., 2005), β is defined as the angle of steepest decent calculated from the elevation gradient of the longitudinal bed, and α is the angle between the flow-velocity vector, U_b, at the top of the bedload layer and the steepest bed slope.

The Shields parameter in Eq. (8) is defined by

$$\theta = \frac{\|U_f\|^2}{(s-1)gd}, \tag{10}$$

where $s=\rho_s/\rho$ is the specific gravity of the sediment grains, and g is the acceleration of gravity. The friction velocity is determined utilizing a method developed by Nikuradse (1933), which is based on bed roughness in a logarithmic velocity profile:

$$\frac{\langle U \rangle}{U_f} = 2.5 \ln\left(\frac{z}{z_0}\right), \tag{11}$$

where z is the distance to the wall, and z_0 is the distance from the boundary at which point the idealized velocity given by the Wall Law goes to zero, and < > represents time-averaged (Rodi et al., 2013). According to Nikuradse (1933), z_0 is equal to $k_s/30$, in which k_s is the Nikuradse equivalent sand roughness.

In the current study, the bedload is assumed to move in the same direction as the tangential shear stress on the bed. The present bedload model reduces the algorithm to simple calculation as shown by Zhou (2017).

3.3. The sand-slide model

Without a sand-slide model, an unrealistic bed-slope which is larger than the physical value of the angle of repose will occur, and large mesh distortion especially will appear, especially around the vertical cylinder. As a consequence, the sigma-transformation will lose its ability to simulate scour holes. In order to prevent the bed slope from exceeding the sediment angle of repose, a mass-conservation-based algorithm for sand-slide has been applied successfully (Khosronejad et al., 2011, 2012). The bed slope is defined by the elevation gradient between point p and any point i (i=1, 2, 3) of the neighboring cell centers, see Fig. 1(a). If the slope angle exceeds the material angle of repose, the sediment particles will slide down to the angle of repose, see Fig. 1(b). The correction to bed elevations is calculated by:

$$\frac{\left(z_{bp}+\Delta z_{bp}\right)-\left(z_{bi}+\Delta z_{bi}\right)}{\Delta l_{pi}}=\tan\phi, \tag{12}$$

where ϕ is the material angle of repose, z_{bp} and z_{bi} are the bed elevations at points p and its i^{th} neighbor; Δz_{bp} and Δz_{bi} are the corresponding corrections, and Δl_{pi} is the horizontal distance between these two points. The bed elevation corrections are obtained by mass conservation as follows:

$$A_{hp}\Delta z_{bp}-\sum_{i=1}^{3}A_{hi}\Delta z_{bi}=0, \tag{13}$$

where A_{hp} and A_{hi} are the area projection of cells p and i, respectively. Since the mesh points move only in the vertical direction, the bed cells projected onto the horizontal plane have the same cell area.

4. Numerical techniques

The hydrodynamic model solves the three-dimensional Navier-Stokes equations using a projection method combined with a sigma-transformation and a second-order unstructured finite volume method.

4.1. The projection method

In this paper, the projection method developed by Chorin (1968) and Temam (1968) is used to decouple the pressure and the velocity field in solving the Navier-Stokes equations. In Cartesian coordinates, the velocity field is obtained by solving a convection-diffusion equation and then the provisional velocity is projected as

$$\frac{\bar{u}_i^* - \bar{u}_i^n}{\Delta t} + \frac{\partial(\bar{u}_i^* \bar{u}_j^n)}{\partial x_j} = \frac{\partial}{\partial x_j}\left(\upsilon \frac{\partial \bar{u}_i^*}{\partial x_i} - \tau_{ij}^n\right), \quad (14)$$

$$\frac{\bar{u}_i^{n+1} - \bar{u}_i^*}{\Delta t} = -\frac{1}{\rho}\frac{\partial \bar{p}^{n+1}}{\partial x_i}, \quad (15)$$

$$\frac{\partial \bar{u}_i^{n+1}}{\partial x_i} = 0, \quad (16)$$

where n and n+1 represent time t^n and t^{n+1}, respectively, Δt is the time step, and (*) is purely symbolic; designating the velocity values obtained after the first projection step. The combination of the continuity and momentum equations yields the Poisson equation. The sigma-transformation is applied to the projection equations in Cartesian coordinates.

4.2. Sigma-transformation

In order to accurately represent bottom geometry, the sigma-coordinate system developed by Phillips (1957) is applied in the current study. This method is applied in order to link the irregular physical domain to a rectangular computational one (see Fig. 2). The conventional sigma-coordinates map the total water depth which is measured from the mobile bottom to the surface of the water onto a fixed range σ = [0, 1] in the computational domain as follows:

$$x^* = x,\ y^* = y,\ t^* = t,\ \sigma = \frac{z+h}{h}, \quad (17)$$

where $h(x^*,y^*,t^*)$ is the total water depth, and z = [-h,0] is the vertical coordinate in the physical domain with the origin at z_s = 0 on the still water surface level, and z_b = -h on the bed level. The partial differentiation of a variable φ in the physical domain is transformed as follows:

$$\frac{\partial \varphi}{\partial t} = \frac{\partial \varphi}{\partial t^*} + \sigma_t \frac{\partial \varphi}{\partial \sigma}, \quad (18)$$

$$\frac{\partial \varphi}{\partial x} = \frac{\partial \varphi}{\partial x^*} + \sigma_x \frac{\partial \varphi}{\partial \sigma}, \quad \frac{\partial \varphi}{\partial y} = \frac{\partial \varphi}{\partial y^*} + \sigma_y \frac{\partial \varphi}{\partial \sigma}, \quad \frac{\partial \varphi}{\partial z} = \sigma_z \frac{\partial \varphi}{\partial \sigma}, \tag{19}$$

where

$$\sigma_t = \frac{1}{h}(1-\sigma)\frac{\partial h}{\partial t^*}, \tag{20}$$

$$\sigma_x = \frac{1}{h}(1-\sigma)\frac{\partial h}{\partial x^*}, \quad \sigma_y = \frac{1}{h}(1-\sigma)\frac{\partial h}{\partial y^*}, \quad \sigma_z = \frac{1}{h}. \tag{21}$$

The foregoing transformation can then be applied to all the terms in the mass and momentum equations and further details can be found in the work of Uh Zapata et al. (2014).

4.3. Finite volume discretization

A second-order unstructured finite volume method (UFVM) is chosen to discretize the Navier-Stokes equations using a cell-center collocated grid with auxiliary vertex points. The 3D domain in sigma-coordinates is discretized into prisms: triangular elements in the horizontal axis and layers in the vertical axis. Thus, each prism-shaped control volume, V, has five faces S_l (l=1,…,5).

A UFVM for the Poisson equation has already been developed and tested by the authors of this study in a previous work (Uh Zapata et al., 2014). The implicit Runge-Kutta time-advancement scheme for the momentum equation of any velocity component in the projection method can be written as follows:

$$\int_V \overline{u}_i^* dV + \Delta t \sum_{l=1}^{5} \int_{S_l} \left[\overline{u}_i^* \overline{u}_j^n - \upsilon \frac{\partial \overline{u}_i^*}{\partial x_i} + (\tau_i^{sg})^n \right] n_l dS = \int_V \overline{u}_i^n dV \,, \tag{22}$$

where n_l is the outward normal unit vector at each face S_l. By the requirements of the LES technique and to preserve second order accuracy, advection terms are handled by a centered scheme. The Momentum Interpolation Method (Rhie & Chow, 1983) is applied to prevent a checkerboard pattern in the pressure field by using a collocated grid. The discretization of the diffusive fluxes involves knowledge of the derivatives at the interface between two neighboring control volumes. In the current study, these derivatives are approximated as an average over a prism-shape, delimited by the two cell-centered points and the vertex of the interface. Thus, the finite volume discretization of the diffusion term relates an unknown value not only with its surrounding cell-centered values, but also with the vertex values of a control volume. The value at any vertex is obtained by averaging over all surrounding cell-centered nodal values.

The morphodynamic model, given by Eq. (7), is integrated on each triangular element. After application of Green's theorem, the integral form of the right-hand side becomes:

$$\iint_A \frac{z_b^{n+1} - z_b^n}{\Delta t} dS = -\frac{1}{(1-\eta)} \sum_{j=1}^{3} \int_{L_j} q_b \cdot n_j dl \; , \qquad (23)$$

where A indicates a triangular element, while L_j and n_j (j=1,2,3) represent an edge and the corresponding unit normal vector of the triangular element.

Boundary conditions are integrated into the problem by updating the ghost cell-centered values. In other words, the total number of unknowns includes not only the values at the cell-centered points inside the domain, but also the ghost points outside of the domain. In the case of Dirichlet boundary conditions, known values are directly applied at vertex points and included at the cell-centered points. In the case of Neumann conditions, approximations can easily be applied for the cell-centered points using a central approximation. However, there is no direct way to apply this condition at vertex values due to the unstructured grid. The vertex values are update exclusively using an interpolation technique.

The current code is fully parallelized using the domain decomposition scheme and Message Passing Interface (MPI) (Uh Zapata et al., 2016), and the code is fully tested on Électricité de France (EDF)-France ATHOS high performance computers (Intel Xeon E 22000 CPUs).

5. Numerical simulations

A sketch of the computational geometry for the numerical simulations around a circular cylinder is shown in Fig. 3. The computational domain extends 10*D* upstream, 20*D* downstream and 30*D* lateral from the cylinder, in which *D* is the cylinder diameter. The origin of the coordinate system is located at the bottom of the cylinder's center, with the *x*, *y*, and *z* axes corresponding to the streamwise, spanwise, and ascendant vertical direction, respectively. The calculation domain is discretized into the order of three million finite volumes with a fine resolution at the HV system region around the cylinder and close to the bed in the vertical direction. Horizontally, the first row of elements is situated at 0.003*D* away from the cylinder surfaces corresponding to 14 wall units. A detailed view of the deformed mesh close to the cylinder is shown in Fig. 4.

The boundary conditions for the flow field are defined as follows: at the inlet, transverse and vertical velocities are specified as zero. The inflow velocity is given by a Poiseuille profile with a unit mean non-dimensional value and boundary layer thickness δ/D = 0.5. At the outlet, zero-gradient conditions were applied for all variables. The boundary in the spanwise direction is set as Neumann conditions. As was pointed out in the previous section, a rigid surface is used on the top. Finally, no-slip wall boundary conditions are applied for the cylinder surface and the bottom bed.

In the current paper, a numerical study similar to Roulund et al. (2005) is done. The diameter of the cylinder is D = 0.1m. The water depth is set to be h = 4D. The undisturbed mean flow velocity is U = 0.46*m/s*. The sand size is d = 0.26*mm*. The equivalent roughness height for the rough wall function is set to be k_s = 2.5d, which determines the skin friction velocity in turn. In the current study, three kinds of calculations are done: a free slip bed with Reynolds number Re_D = 3,900 is done in order to validate the results with experimental data; rigid bed calculations with Re_D = 46,000 is applied to investigate the flow features only*;* and a live bed scour with Re_D = 46,000 is applied to test the morphological model. The initial condition for live bed scour is derived from the final results of the rigid bed simulation. The conditions in the last two cases are summarized in Table 2.

5.1. Free slip bed simulation results using Re_D = 3,900

In order to validate the proposed model, a comparison between numerical and experimental results is presented for a free slip bed at Re_D = 3,900 and the bottom boundary condition is set as free-slip. The vertical mean streamwise (u/U) and spanwise (v/U) velocity components at five different stations, x = 1.06, 2.02, 3.0, 4.0, and 5.0, are plotted in Fig. 5. A U-shaped profile is observed near the wake region. The experimental data LS93 and OW93 were obtained from Lourenco (1993) and Ong and Wallace (1996), respectively. LES B16 corresponds to numerical results from Bai et al. (2016). It can be seen that the numerical results largely correlate with the experimental data, except at x = 1.06, where the uncertainties in the measurements are high. For the purpose of demonstrating this discrepancy, the numerical result obtained by Tremblay et al. (2000) using Direct Numerical Simulation (DNS) is also included in Fig. 5(b). It can be seen that the current numerical results actually are very close to the DNS prediction.

5.2. *Rigid bed flow simulation results using Re_D = 46,000*

5.2.1. Shear stress validation

Figure 6 shows the bed shear-stress iso-values, obtained from the mean flow simulation and compared with the results of Roulund et al. (2005). The model reproduces most of the characteristics observed by Roulund et al. (2005) in the vicinity of the cylinder but with very slight discrepancies far away from it. The average distribution of the shear stress is fairly axisymmetric. High values are found for shear stress on the two sides close to the cylinder, approximately corresponding to the position where the velocity is highest, just before the flow separation line.

5.2.2. Horseshoe vortex system

The HV system is attributable to the separation of the incoming boundary layer induced by adverse pressure gradients, which are generated by the cylinder obstruction. The turbulence driven by the resulting flows will result in a number of necklace-like structures around the upstream side of the cylinder. Because of the lateral pressure gradients, these structures stretch when they fold around the cylinder (Kirkil et al., 2008). Their legs are approximately parallel to the direction of the incoming flow. Figure 7 shows the main coherent structures in an instantaneous flow associated with a HV system on a rigid bed withg $h = 4D$ and Re_D = 46,000. Clearly two primary necklace vortices and two bottom-attached vortices are present. A U-shaped Primary Vortex (PV1) wraps around the upstream part of the cylinder, along which a small, but very coherent, junction vortex appears at the base of the cylinder (JV). Another U-shaped Primary Vortex (PV2) is observed upstream of PV1. The formation of Bottom-Attached Vortices, BAV1 and BAV2, are induced upstream by the presence of the primary vortices PV1 and PV2. Secondary Vortices (SV1) are observed towards PV2.

The location, size, and intensity of the turbulent HV greatly vary in time. Figure 8 shows four instances of a cycle of oscillation. The main vortex cores occur in different positions. Clockwise-rotating primary vortices (PV1, PV2) and counter-rotating bottom-attached vortices (BAV1, BAV2) appear at all times during the oscillation cycle, exhibiting a relatively stable behavior. Smaller secondary vortices (SV) shed randomly from the separation region of the incoming boundary layer. These SV are convected toward PV2 and can interact and merge with it. The direction of the oscillation centers of PV1 and PV2 are found to be oppositely positioned to one another: at $t = T/2$ they move closer, and at $t = T/4$ and $t = 3T/4$ they move far away from each other. The amplitude of oscillation in the direction of flow is about $0.1D$. The structure of the HV system, observed in the results of current model using $h = 4D$ and $Re_D = 46{,}000$, is similar to the ones of Kirkil et al. (2008) using $h = 1.12D$ and $Re_D = 16{,}000$.

5.2.3. Near wake flow

Figure 9 shows mean streamlines on a longitudinal plane located behind the cylinder in the wake. *S*, *F*, and *N* denote the saddle points, the centers of foci, and nodal points, respectively. The arrows represent the direction of the flow. It is noticed that a nodal point of attachment N_1 is present, corresponding to the merging point of shear layers emanating from both sides of the vertical cylinder to form a spanwise-oriented vortex. As a consequence, fluid particles situated close to the bed are first entrained into the core of this vortex, and then from there toward the surface by an upwelling anti-clockwise vortex, shown by a foci point, F_1. This counter-clockwise rotating vortex is responsible for the scour mechanisms downstream of the cylinder.

Figure 10 shows mean flow streamlines on different spanwise cross sections located at four different stations: x/D = 0.5, 1.0, 1.5, and 2.0. The streamline patterns are almost symmetric, except for the lee wake just behind the cylinder. A pair of vortices is present near the bed corresponding to the primary vortex legs. It can be seen that even at $x = 2D$, these legs are still present. The shear layers, emanating from the side edges of the cylinder, roll up to form vortices in the lee wake of the cylinder. These vortices engender upwelling motion of fluid particles toward the surface. The upwelling motion inside the wake region is compensated by downwelling motion on the outside.

Figure 11 shows mean flow streamlines on horizontal planes at z/D = 0.05, 1.0, and 2.0 in the wake region. The flow separation points are located at φ = 90°, 105°, and 110° at z/D = 0.05, 1.0 and 2.0, respectively. It can be seen that these separation points move downstream as z/D increases. This observation is also noted by Kirkil and Constantinescu (2015). Moreover, Figure 11 shows that the wake region becomes bigger as it rises to the surface. Saddle points, S_2 and S_3 indicate the end of the wake region at planes z/D = 0.05 and 1.0 and the corresponding detachment lengths are 0.9D and 1.9D, respectively. Foci points F_4 (x = 0.55, y = 0.13), F_5 (x = 1.24, y = 0.2) and F_6 (x = 2.05, y = -0.22) show the position of upwelling vortices V_1, V_2, and V_3.

5.3. Live bed scour simulation results at Re_D = 46,000

5.3.1. Horseshoe vortex system

Figure 12 shows the main necklace vortices inside the scour hole by using the Q criterion. Similar to the rigid bed case, U-shaped necklace vortices also appear in the live bed case. They contain two Primary Vortices (PV1 and PV2), a Bottom-Attached Vortex (BAV), and a Joint Vortex (JV) (Dey & Raikar, 2007). The HV system is closely related to the scour process. According to Baker (1979) and Kirkil et al. (2008), the number of these necklace vortices and their extent in the polar direction may change with the Reynolds number. Necklace-like structures detach from the incoming bottom boundary layer over a certain range of polar angles and then interact with other secondary vortices or with the primary one. Some of these vortices merge with the main or another secondary necklace vortex; others will lose their coherence rapidly. Consequently, the intensity of the overall HV system varies substantially over time. In many cases, the interaction with another necklace structure takes place only over a limited area of the total length of two vortices.

Figure 13 provides more details on the temporal evolution of the streamlines in the scour hole upstream from the cylinder. The current model successfully simulates the dynamics of the initial stages of erosion by the unsteady coherent structures of the HV system. As the scour hole gets deeper and extends, the HV system grows in size but decreases in strength until reaching the conditions for equilibrium. Such a state of equilibrium is reached when the shear stresses are reduced down to a local threshold value for sediment-particle entrainment. Once the scour hole has formed, the HV system becomes more stable. During the scour process, PV1 still oscillates around at $x = 0.5D$ upstream the cylinder, as for the rigid bed case, and slips down into the middle of the hole to adapt to a new position in the bed. PV2 grows bigger and increases in coherence. With the development of PV1 and PV2, a BAV is generated and grows between them. The vortices corresponding to JV grow bigger as the scour domain develops close to the cylinder.

5.3.2. Near wake flow

Figure 14 shows time-averaged streamlines for the live bed case on a longitudinal plane behind the cylinder in the wake region. A large recirculation zone is generated due to the changes in bed topography as the flow moves downstream. As with the rigid bed cases, a nodal point, N_2, of attachment positioned at (x/D = 0.875, z/D = -0.1785) exists. The negative sign indicates that this level is below the initial bed level. N_2 corresponds to the merging point of the streamlines issued from the convergence of both lateral sides of the cylinder. Thus, sediment particles situated close to the bed are entrained by the flow: first in the spanwise direction and later toward the surface by an upwelling anti-clockwise vortex, indicated by foci F_7. The presence of foci and nodal points in the wake region has already been observed in experimentation using $h = 6D$ and $Re_D = 7000$ (Sahin & Ozturk, 2009).

Figure 15 shows a 3D view of time-averaged streamlines around the cylinder. Clearly, a down flow can be observed at the upstream side of the cylinder which generates a primary vortex, as discussed in the preceding paragraphs. The flow structure in the wake region also is shown in this figure. Streamlines wrap the cylinder from both lateral sides. Then, flow in the spanwise direction converges at nodal point N_2. From N_2, due to an upwelling vortex (F_7), an important patch of fluid rises up into the surface layers, entraining sediment particles situated on the bed, and bringing them out of the wake. This phenomenon induces the scour process behind the cylinder.

5.3.3. General erosion patterns and maximum erosion depth prediction

Figure 16 shows the evolution of the scour hole over time as obtained by the proposed model at four times: 30 *s*, 120 *s*, 300 *s* and 750 *s*. The pattern exhibited by the scour hole closely resembles the results observed by Roulund et al. (2005). The deepest part of the main scour hole occupies the upstream and spanwise sides of the cylinder. A maximum angle for the bed slope is fixed inside this region, equal to the prescribed angle of repose: 32°. The exact localization of the maximum angle corresponds to regions where the sand-slide algorithm fuctions and where the avalanching process is yielded by the model. Additionally, sand particles are deposited downstream from the cylinder. Some small bed changes are observed far from the main scour hole. The evolution of sand deposition downstream from the cylinder is almost symmetric with the presence of sandpits. These sandpits tend to decrease with time without being fully erased at $t = 750s$.

Figure 17 shows the time evolution of the scour depth at the upstream and downstream sides of the cylinder compared with the measurements of Roulund et al. (2005). At the beginning of the scour, both numerical models slightly over-predict the depth at the upstream side while under-predicting the depth at the downstream side compared to the experimental data. Roulund et al. (2005) explained the reasons for the downstreram discrepancy between simulation and experimental results. One reason is that the suspended load process is not included in the model, therefore, the model scour depth remains rather small during this stage. Another reason is that the vortex shedding in the lee wake of the cylinder is ignored, which will decrease the predicted scour depth downstream of the cylinder (Sumer et al., 1988). Here, the second factor has been taken into consideration in the proposed model. Clearly, the current numerical results on the hole evolution are in a better agreement with the experimental results both in the upstream and downstream directions, compared with those of Roulund et al. (2005). The simulation results from Roulund et al. (2005) have reached the equilibrium condition at about 1000 s, but with scour depth values are smaller than the experimental results. The current results are closer to the experimental results in both upstream and downstream locations.

6. Conclusions and future work

A Navier-Stokes solver based on the projection method and a second-order unstructured finite-volume mesh, using LES is proposed to simulate the hydrodynamics and the scour process around a circular cylinder. A sigma-coordinate system is applied to follow the sediment-water interface. Bed erosion is simulated by solving the sediment continuity equation in the bedload layer using a mass-conservation-based algorithm for sand-slide and a bedload transport rate based on a description of the physical processes (Engelund & Fredsøe, 1976). The proposed model has been rigorously validated for the free slip bed case and the rigid bed case through comparison with previous studies. Then, the simulation of the scour process around a cylinder for the live bed case with h = 4D and Re_D = 46,000 is then done. The current study focused on the coherent structure of the flow fields at the beginning stage of the scour process.

In the free slip bed case, mean streamwise and spanwise velocity profiles on a rigid bed at different streamwise positions are in good agreement with measurements. In the rigid bed case, the proposed model reproduces shear stress observed by Roulund et al. (2005) in the vicinity of the cylinder but with a very slight discrepancy far away from it. The HV system is relatively stable and under an oscillating cycle. It is composed of primary, bottom-attached and secondary necklace vortices and a small coherent junction votex. For h = 4D and Re_D = 46,000, there are two primary and two bottom-attached vortices in the instantaneous flows. During an oscillation cycle, the two primary vortices move in opposite directions, and in the end, they return to approximate their initial positions. The oscillating distance is about 0.1D. The legs of the primary vortices are nearly parallel to the incoming flow and they are still present downstream from the cylinder until the position x = 2D. Indeed, the HV structure in the documented case has almost the same structure as that for Kirkil et al. (2008) for h/D = 1.12.

In the live bed case, the HV system is closely related to the scour process. It is unstable at the initial stage of scour and then becomes more stable as the scour hole is formed. The obstruction caused by the cylinder generates the local redistribution of pressure and induces down flows at the upstream face of the cylinder generating primary vortices. Streamlines wrap the cylinder from both lateral sides, converging at a nodal point downstream. From there, due to an upwelling vortex, fluids rise up to the surface, entraining the sediment particles situated on the bed, bringing them downstream to deposit somewhere else. This generates the scour process behind the cylinder.

Acknowlegments

The authors gratefully acknowledge the ANR SSHEAR project (No.2014-CE03-0011), the Mexican Council of Science and Technology project (CONACYT No. 256252) and the Chinese Scholarship Council (CSC) for the financial support to do this work. The authors extend special thanks to Électricité de France Recherche & Dévelopment (EDF R&D) for their support in providing the access to the computing facilities.

References

Bai, W., Mingham, C. G., Causon, D. M., & Qian, L. (2016). Detached eddy simulation of turbulent flow around square and circular cylinders on Cartesian cut cells. *Ocean Engineering*, *117*, 1–14.

Baker, C. J. (1979). The laminar horseshoe vortex. *Journal of Fluid Mechanics*, *95*(02), 347–367.

Baykal, C., Sumer, B. M., Fuhrman, D. R., Jacobsen, N. G., & Fredsoe, J. (2014). Numerical investigation of flow and scour around a vertical circular cylinder. *Philosophical Transactions of the Royal Society A: Mathematical, Physical and Engineering Sciences*, *373*(2033), 104.

Baykal, C., Sumer, B. M., Fuhrman, D. R., Jacobsen, N. G., & Fredsøe, J. (2017). Numerical simulation of scour and backfilling processes around a circular pile in waves. *Coastal Engineering*, *122*, 87–107.

Chorin, A. J. (1968). Numerical solution of the Navier-Stokes equations. *Mathematics of Computation, 22*(104), 745–762.

Dargahi, B. (1990). Controlling mechanism of local scouring. *Journal of Hydraulic Engineering, 116*(10), 1197–1214.

Deardorff, J. W. (1970). A numerical study of three-dimensional turbulent channel flow at large Reynolds numbers. *Journal of Fluid Mechanics, 41*(02), 453–480.

Dey, S., & Raikar, R. V. (2007). Characteristics of horseshoe vortex in developing scour holes at piers. *Journal of Hydraulic Engineering, 133*(4), 399–413.

Engelund, F., & Fredsøe, J. (1976). A sediment transport model for straight alluvial channels. *Hydrology Research, 7*(5), 293–306.

Fernandez Luque, R., & van Beek, R. (1976). Erosion and transport of bed-load sediment. *Journal of Hydraulic Research, 14*(2), 127–144.

Khosronejad, A., Kang, S., Borazjani, I., & Sotiropoulos, F. (2011). Curvilinear immersed boundary method for simulating coupled flow and bed morphodynamic interactions due to sediment transport phenomena. *Advances in Water Resources, 34*(7), 829–843.

Khosronejad, A., Kang, S., & Sotiropoulos, F. (2012). Experimental and computational investigation of local scour around bridge piers. *Advances in Water Resources, 37*, 73–85.

Kirkil, G., Constantinescu, S. G., & Ettema, R. (2008). Coherent structures in the flow field around a circular cylinder with scour hole. *Journal of Hydraulic Engineering, 134*(5), 572–587.

Kirkil, G., & Constantinescu, G. (2010). Flow and turbulence structure around an in-stream rectangular cylinder with scour hole: Flow around a rectangular culinder. *Water Resources Research, 46*(11).

Kirkil, G., & Constantinescu, G. (2015). Effects of cylinder Reynolds number on the turbulent horseshoe vortex system and near wake of a surface-mounted circular cylinder. *Physics of Fluids, 27*(7), 075102.

Link, O., González, C., Maldonado, M., & Escauriaza, C. (2012). Coherent structure dynamics and sediment particle motion around a cylindrical pier in developing scour holes. *Acta Geophysica, 60*(6), 1689–1719.

Lourenco, L. M. (1993). Characteristics of the plane turbulent near wake of a circular cylinder. *A Particle Image Velocimetry Study*. Retrieved from https://ci.nii.ac.jp/naid/10009520643/en/

Mason, P. J., & Thomson, D. J. (1992). Stochastic backscatter in large-eddy simulations of boundary layers. *Journal of Fluid Mechanics, 242*(1), 51.

Meland, N., & Norrman, J. O. (1966). Transport velocities of single particles in bed-load motion. *Geografiska Annaler. Series A, Physical Geography, 48*(4), 165.

Melville, B. W., & Chiew, Y.-M. (1999). Time scale for local scour at bridge piers. *Journal of Hydraulic Engineering, 125*(1), 59–65.

Nagel, T. (2018). Numerical study of multi-scale flow-sediment-structure interactions using a multiphase approach (*Ph.D. dissertation*), Laboratoire des Écoulements Geophysiques et industrials, Université Grenoble Alpes. Retrieved from https://tel.archives-ouvertes.fr/tel-01920495/

Nikuradse, J. (1933). Laws of flow in rough pipes. *Technical Memorandum 1292.* Washington: National Advisory Committee for Aeronautics.

Nishioka, M., & Sato, H. (1974). Measurements of velocity distributions in the wake of a circular cylinder at low Reynolds numbers. *Journal of Fluid Mechanics, 65*(01), 97–112.

Ong, L., & Wallace, J. (1996). The velocity field of the turbulent very near wake of a circular cylinder. *Experiments in Fluids*, *20*(6), 441–453.

Park, J., Kwon, K., & Choi, H. (1998). Numerical solutions of flow past a circular cylinder at Reynolds numbers up to 160. *KSME International Journal*, *12*(6), 1200–1205.

Pham Van Bang, D., Lefrançois, E., Sergent, P., & Bertrand, F. (2008). Expérimentation par IRM et modélisation par éléments finis de la sédimentation-consolidation des vases. *La Houille Blanche*, (3), 39–44. (in French)

Phillips, N. A. (1957). A coordinate system having some special advantages for numerical forecasting. *Journal of Meteorology*, *14*(2), 184–185.

Rhie, C. M., & Chow, W. L. (1983). Numerical study of the turbulent flow past an airfoil with trailing edge separation. *AIAA Journal*, *21*(11), 1525–1532.

Rodi, W., Constantinescu, G., & Stroesser, T. (2013). *Large-eddy simulation in hydraulics*. Boca Raton: CRC Press.

Roulund, A., Sumer, B. M., Fredsøe, J., & Michelsen, J. (2005). Numerical and experimental investigation of flow and scour around a circular pile. *Journal of Fluid Mechanics*, *534*, 351–401.

Sahin, B., & Ozturk, N. A. (2009). Behaviour of flow at the junction of cylinder and base plate in deep water. *Measurement*, *42*(2), 225–240.

Smagorinsky, J. (1963). General Circulation Experiments with the Primitive Equation: I. the Basic Experiment. *Monthly Weather Review*, *91*(3), 99–164.

Stahlmann, A. (2013). Numerical and experimental modeling of scour at foundation structures for offshore wind turbines. Presented at the International Society of Offshore and Polar Engineers, Poland. Retrieved from http://www.isope.org/publications

Sumer, B. M., Jensen, H. R., Mao, Y., & Fredsøe, J. (1988). Effect of lee-wake on scour below pipelines in current. *Journal of Waterway, Port, Coastal, and Ocean Engineering, 114*(5), 599–614.

Temam, R. (1968). Une méthode d'approximation de la solution des équations de Navier-Stokes. *Bulletin de La Société MathéMatique de France, 96*, 115–152. (in French)

Tremblay, F., Manhart, M., & Friedrich, R. (2000). LES of flow around a circular cylinder at a cubcritical Reynolds number with Cartesian grids. *8th EuropeanTurbulence Conference,* (pp.659–662), Barcelona, Spain.

Uh Zapata, M., Pham Van Bang, D., & Nguyen, K. D. (2014). An unstructured finite volume technique for the 3D Poisson equation on arbitrary geometry using a sigma-coordinate system. *International Journal for Numerical Methods in Fluids, 76*(10), 611–631.

Uh Zapata, M., Pham Van Bang, D., & Nguyen, K. D. (2016). Parallel SOR methods with a parabolic-diffusion acceleration technique for solving an unstructured-grid Poisson equation on 3D arbitrary geometries. *International Journal of Computational Fluid Dynamics, 30*(5), 370–385.

Williamson, C. H. K. (1989). Oblique and parallel modes of vortex shedding in the wake of a circular cylinder at low Reynolds numbers. *Journal of Fluid Mechanics, 206*(1), 579–627.

Yalin, M. S. (1977). Mechanics of sediment transport (2d ed). Oxford ; New York: Pergamon Press.

Zhou, L. (2017). Numerical modelling of scour in steady flows (*Ph.D. dissertation*), Laboratoire de Mécanique des Fluides et d'Acoustique, École Centrale de Lyon. Retrieved from https://tel.archives-ouvertes.fr/tel-01598600

Figure legends:

Fig. 1. Sand-slide algorithm: (a) an unstructured triangular bed mesh, and (b) definition of quantities used to adjust the computed bed slope.

Fig. 2. Sigma-transformation links irregular domain to a rectangular one.

Fig. 3. Sketch of the geometry of the computational domain and specification of the boundary conditions.

Fig. 4. Detailed view of the deformed mesh close to the cylinder with scouring.

Fig. 5. Mean velocity on a free slip bed at different streamwise positions (*x/D)* using Re_D = 3,900 (a) streamwise (*u/U*) and (b) spanwise (*v/U*) velocities.

Fig. 6. Non-dimensional bed shear stress distribution at Re_D=46,000. (a) Results from Roulund et al. (2005) and (b) current numerical simulation.

Fig. 7. Detailed view of the coherent structure with a HV system on a rigid bed.

Fig. 8. Instantaneous streamlines on the longitudinal section upstream of the cylinder at five instants in time for the rigid bed case.

Fig. 9. Mean flow streamlines on the longitudinal section behind the cylinder for the rigid bed case. The direction of the flow is indicated by the arrows.

Fig. 10. Mean flow streamlines on the vertical cross sections behind the cylinder for the rigid bed case.

Fig. 11. Mean streamlines on different horizontal planes for the rigid bed case.

Fig. 12. Visualization of the main necklace vortices inside the scour hole for the live bed case.

Fig. 13. Horseshoe vortex system in the scour hole development around and in front of the cylinder for the live bed case.

Fig. 14. Time-averaged streamlines on the longitudinal section behind the cylinder for the live bed case.

Fig. 15. 3D time-averaged streamlines of the mean flow for the live bed case.

Fig. 16. Instantaneous images of the bed elevation, showing the evolution of the scour hole around the cylinder.

Fig. 17. Numerical (Num.) and experimental (Exp.) results of the scour depth evolution at the (a) upstream and (b) downstream side of the cylinder for the live bed case.

Table

Table 1. List of methods used in scour simulations in different references

Reference	Numerical model	Turbulence model	Sand slide model	Water-sediment interface	Re_D	Physical phenomenon
Roulund (2005)	Structured finite volume method (FVM)	RANS (k-ω)	Updated particle velocity	Multigrid mesh	4.6×10^4	Scour hole evolution (Live bed erosion)
Kirkil (2008, 2010,2015)	Structured finite volume method (FVM)	LES	Fixed bed (no)	Fixed bed (no)	1.6×10^4	HV system No scour evolution
Khosronejad (2012)	Unstructured finite volume method (UFVM)	RANS (k-ω)	Mass-conservating	FSI-CURVIB	4.95×10^4	Scour hole evolution (Live bed erosion)
Link et al. (2012)	Structured finite volume method (FVM)	DES	No	Lagrangian model	3.15×10^4	Scour hole evolution (Clear-water erosion)
Baykal et al. (2014,2017)	Structured finite volume method (FVM)	RANS (k-ω)	Updated particle velocity	Multigrid mesh	1.7×10^4	Scour hole evolution (Clear-water erosion)
Zhou (2017)	Structured finite volume method (FVM)	RANS (k-ω)	Mass-conservating	Dynamic mesh deformation	4.6×10^4	Scour hole evolution (Live bed erosion)
Nagel (2018)	Structured finite volume method (FVM)	RANS (k-ω)	No	Two-phase model	4.6×10^4	Scour hole evolution (Live bed erosion)
Current paper (2019)	Unstructured finite volume method (UFVM)	LES	Mass-conservating	Sigma transformation	4.6×10^4	HV system Scour evolution (Live bed erosion)

Note: Re_D = Reynolds number

Table 2. Test conditions around a cylinder in the rigid bed and live bed scour cases.

Bed	Loose sand
Water depth, h	0.4 m
Cylinder diameter, D	0.1 m
Boundary layer thickness, δ	0.2 m
Mean flow velocity, U	0.46 m/s
Reynolds number, Re_D	46,000
Froude number, F_r	0.23
Sediment density, ρ_s	2,600 kg/m^3
Fluid density, ρ	1,000 kg/m^3
Grain size, d	0.26 mm
Sand roughness due to skin friction, k_s	0.65 mm

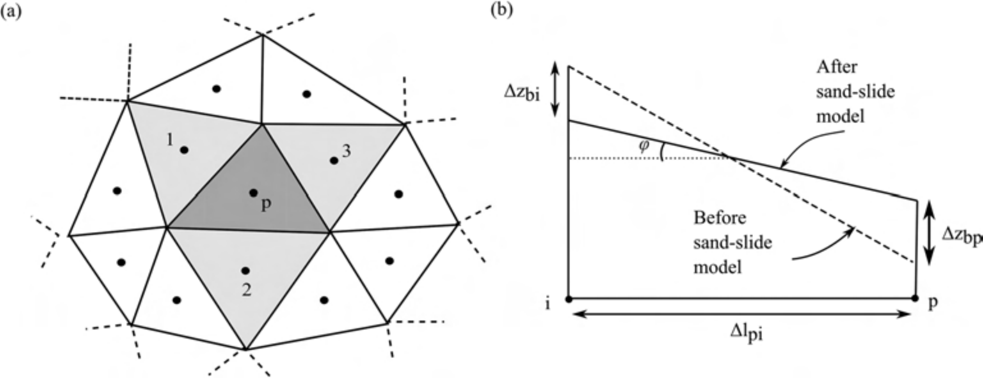

(a)
1
3
p
2
(b)
Δzbi
After
sand-slide
model
φ
Before
sand-slide
model
Δzbp
i
p
Δlpi

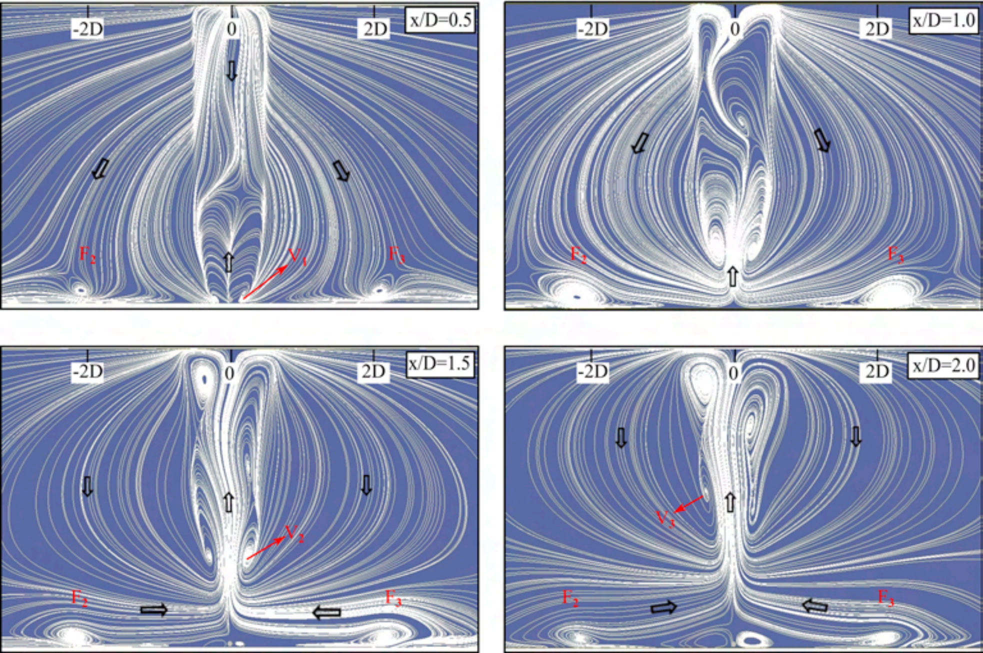

x/D=0.5
x/D=1.0
x/D=1.5
x/D=2.0
-2D
0
2D
F2
F3
V1
V2
V3

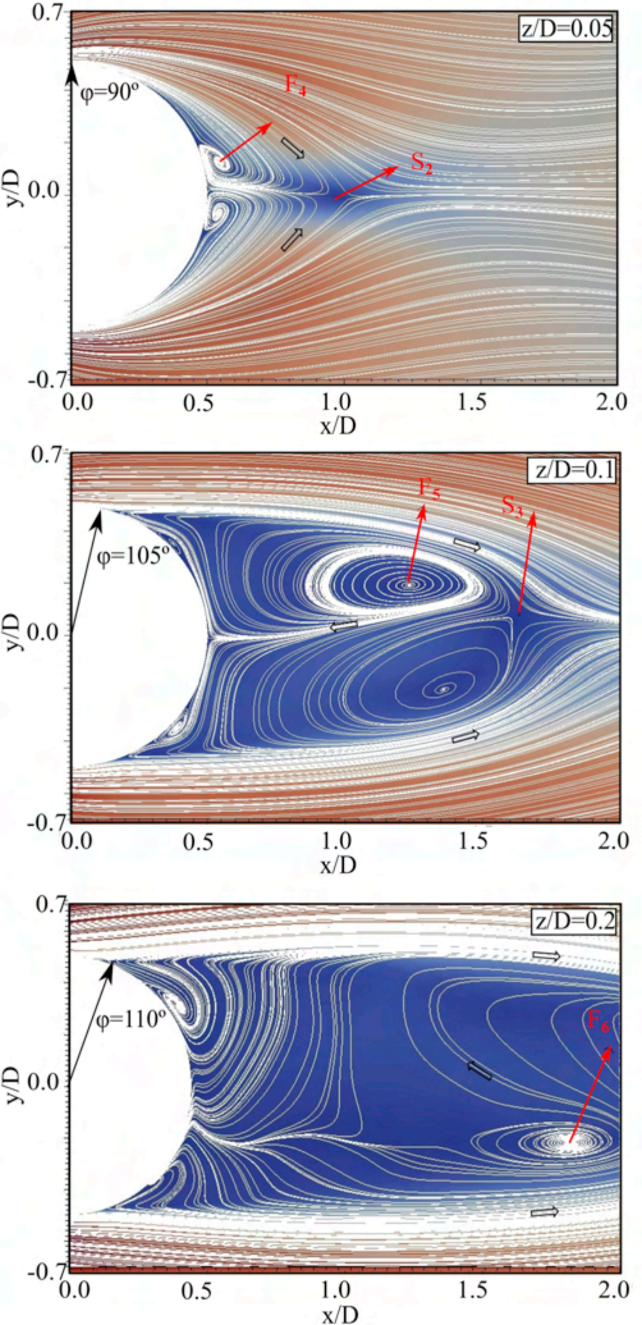

z/D=0.05
φ=90°
F4
S2
z/D=0.1
φ=105°
F5
S3
z/D=0.2
φ=110°
F6
y/D
x/D
0.7
0.0
-0.7
0.0
0.5
1.0
1.5
2.0

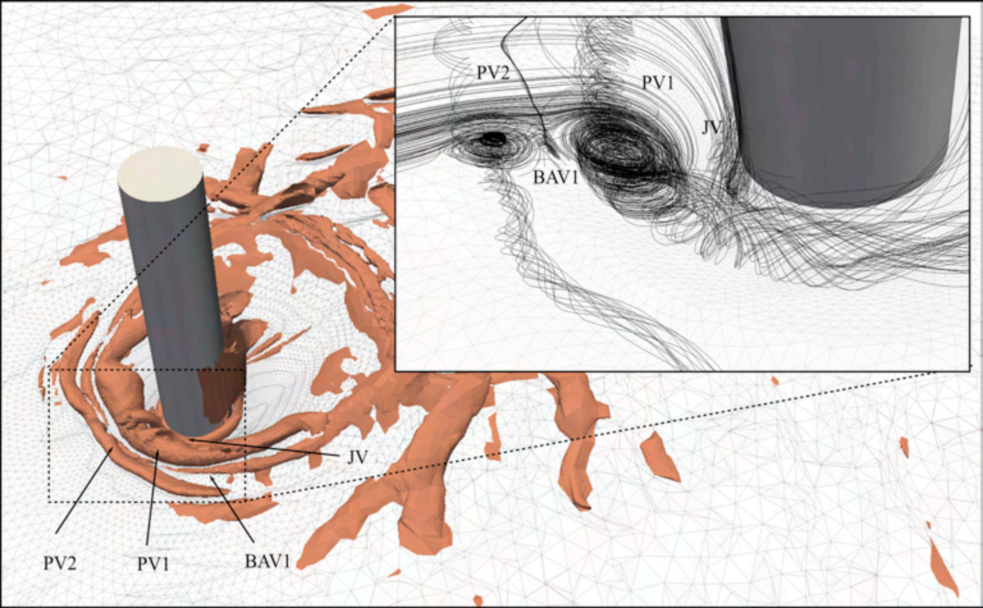
PV2
PV1
JV
BAV1
PV2
PV1
BAV1
JV

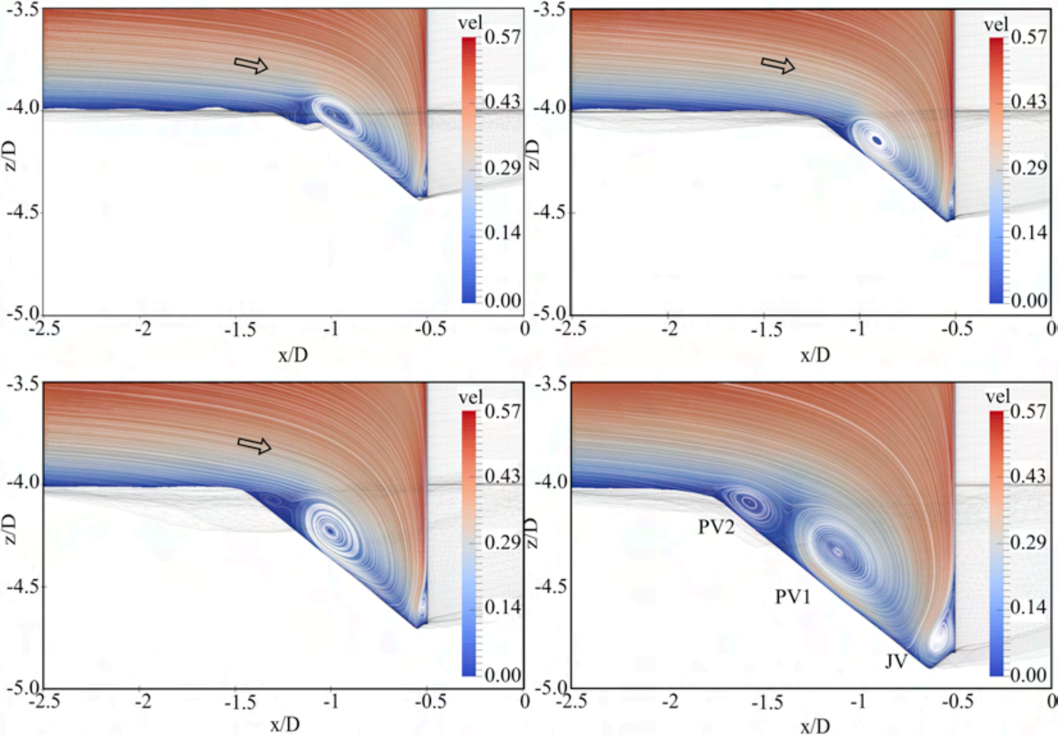

vel
0.57
0.43
0.29
0.14
0.00
z/D
x/D
PV2
PV1
JV

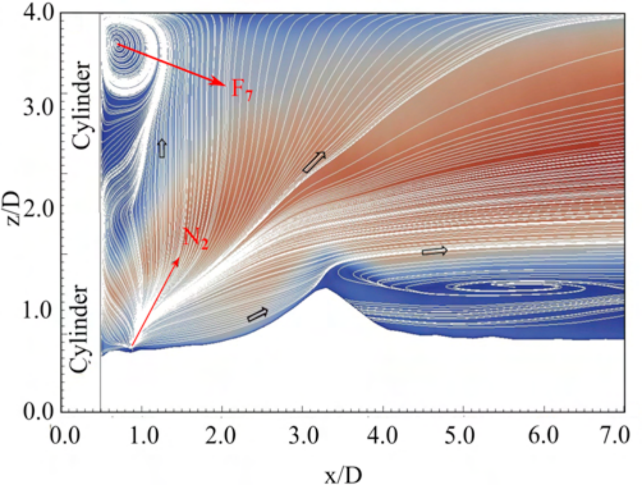

4.0
3.0
2.0
1.0
0.0
z/D
Cylinder
Cylinder
F7
N2
0.0
1.0
2.0
3.0
4.0
5.0
6.0
7.0
x/D

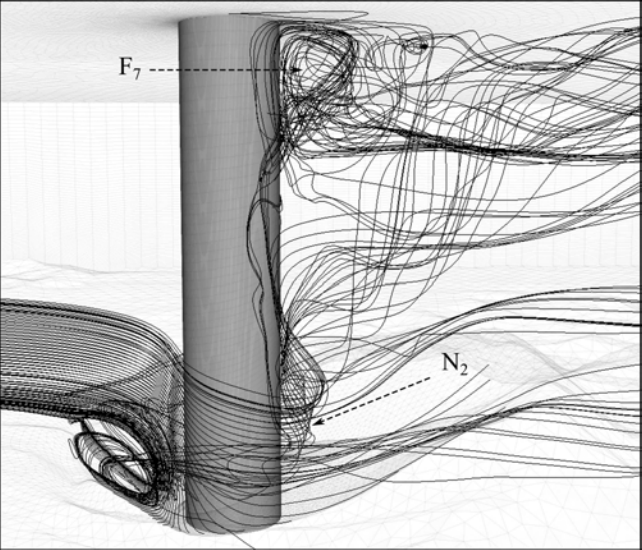
F_7
N_2

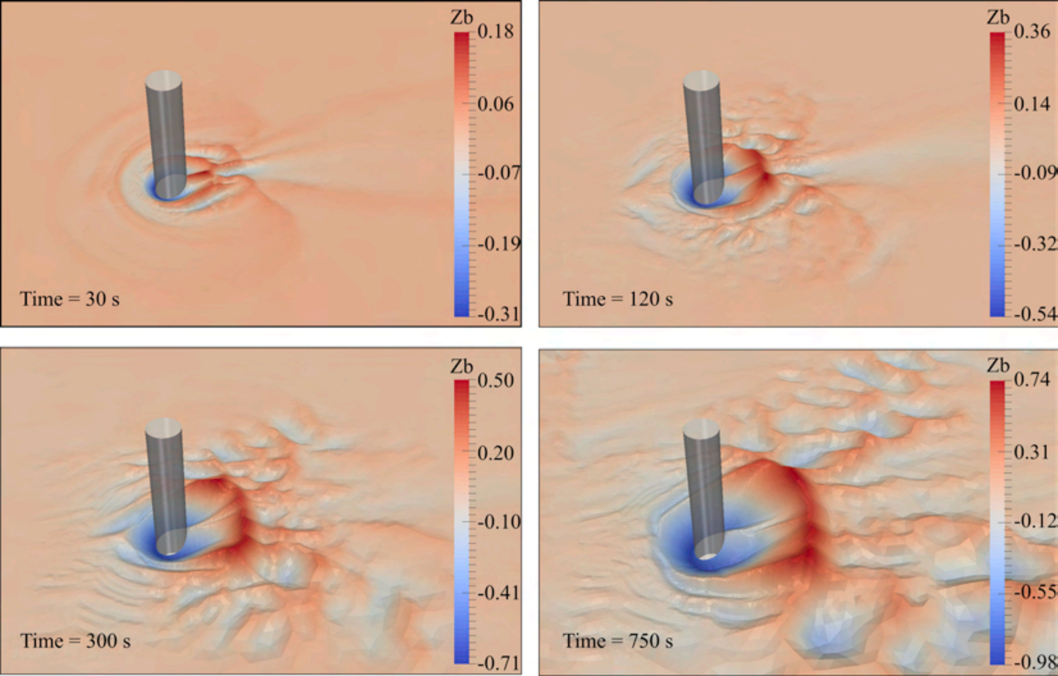

Zb
0.18
0.06
-0.07
-0.19
-0.31
Time = 30 s
Zb
0.36
0.14
-0.09
-0.32
-0.54
Time = 120 s
Zb
0.50
0.20
-0.10
-0.41
-0.71
Time = 300 s
Zb
0.74
0.31
-0.12
-0.55
-0.98
Time = 750 s

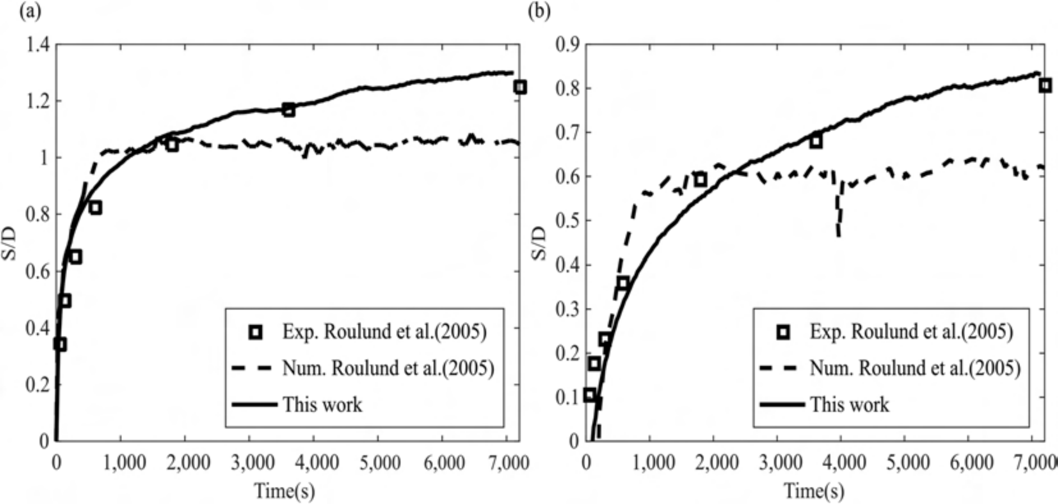

(a)
1.4
1.2
1
0.8
0.6
0.4
0.2
0
S/D
0
1,000
2,000
3,000
4,000
5,000
6,000
7,000
Time(s)
Exp. Roulund et al.(2005)
Num. Roulund et al.(2005)
This work
(b)
0.9
0.8
0.7
0.6
0.5
0.4
0.3
0.2
0.1
0
S/D
0
1,000
2,000
3,000
4,000
5,000
6,000
7,000
Time(s)
Exp. Roulund et al.(2005)
Num. Roulund et al.(2005)
This work

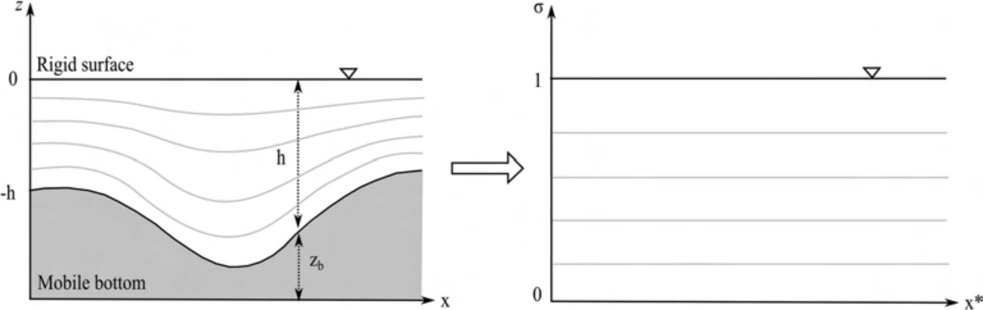
z
Rigid surface
0
h
-h
z_b
Mobile bottom
x
σ
1
0
x*

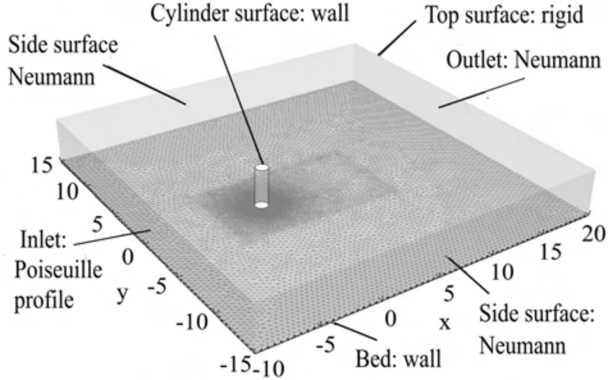

Cylinder surface: wall
Top surface: rigid
Side surface
Neumann
Outlet: Neumann
15
10
5
Inlet:
Poiseuille
profile
0
y
-5
-10
-15
-10
-5
0
5
10
15
20
x
Side surface:
Neumann
Bed: wall

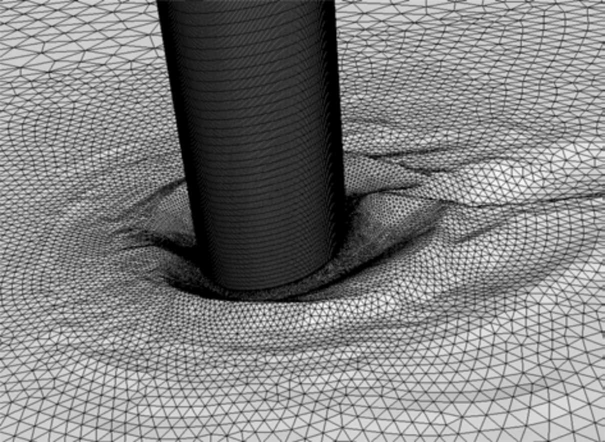

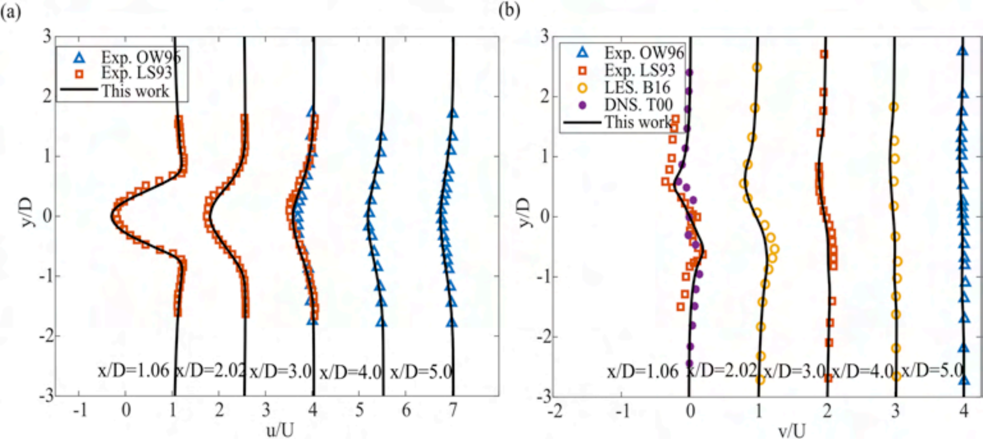

(a)
Exp. OW96
Exp. LS93
This work
y/D
u/U
x/D=1.06 x/D=2.02 x/D=3.0 x/D=4.0 x/D=5.0
(b)
Exp. OW96
Exp. LS93
LES. B16
DNS. T00
This work
y/D
v/U
x/D=1.06 x/D=2.02 x/D=3.0 x/D=4.0 x/D=5.0

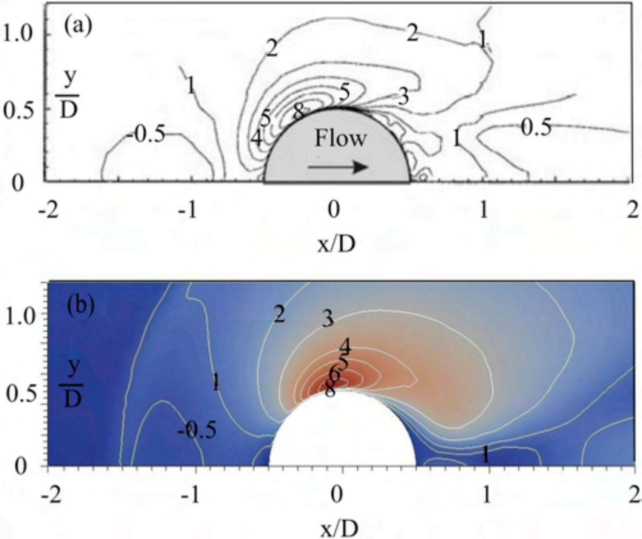
(a)
Flow
2
1
2
1
5
3
8
5
4
-0.5
1
0.5
y/D
x/D
(b)
2
3
4
5
6
8
1
-0.5
1
y/D
x/D

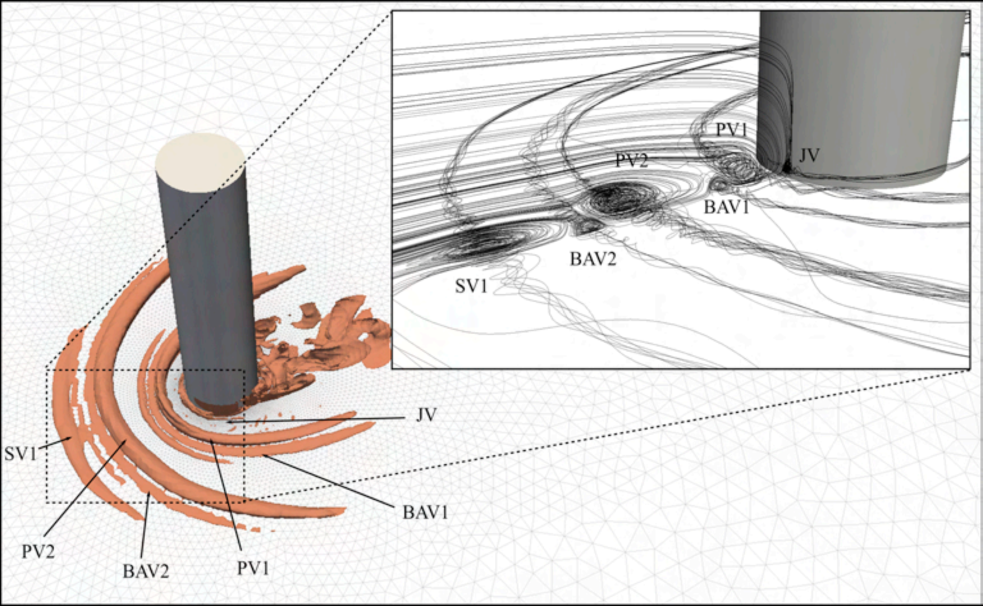
PV1
JV
PV2
BAV1
BAV2
SV1
JV
SV1
BAV1
PV2
BAV2
PV1

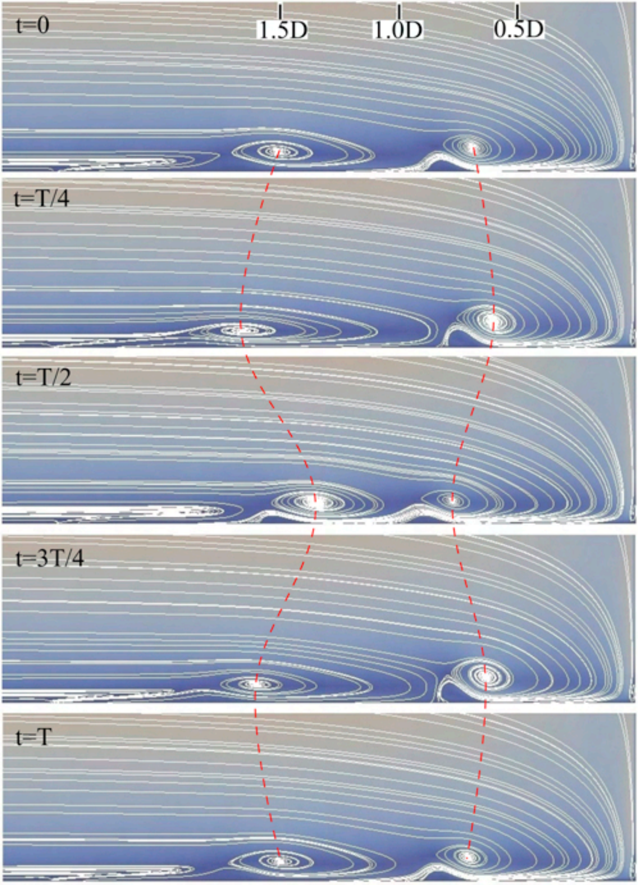
t=0
1.5D
1.0D
0.5D
t=T/4
t=T/2
t=3T/4
t=T

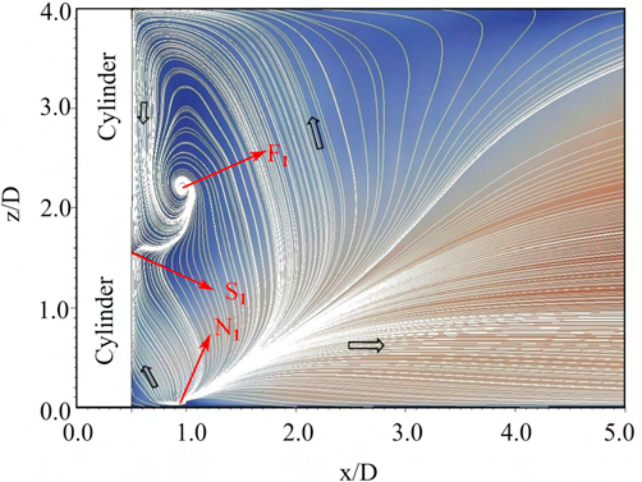

4.0
3.0
2.0
1.0
0.0
z/D
Cylinder
Cylinder
F1
S1
N1
0.0
1.0
2.0
3.0
4.0
5.0
x/D

Conflicts of interest

"**Three-dimensional simulation of horseshoe vortex and local scour around a vertical cylinder using an unstructured finite-volume technique**"

Wei Zhang, Miguel Uh Zapata, Xin Bai, Damien Pham Van Bang, Kim Dan Nguyen

International journal of sediment research 2019

The authors whose names are listed immediately below certify that they have NO affiliations with or involvement in any organization or entity with any financial interest (such as honoraria; educational grants; participation in speakers' bureaus; membership, employment, consultancies, stock ownership, or other equity interest; and expert testimony or patent-licensing arrangements), or non-financial interest (such as personal or professional relationships, affiliations, knowledge or beliefs) in the subject matter or materials discussed in this manuscript.

Wei Zhang, Miguel Uh Zapata, Xin Bai, Damien Pham Van Bang, Kim Dan Nguyen